Release from biogenic particles, benthic fluxes, and deep water circulation control Cr and δ^{53}Cr distributions in the ocean interior

David J. Janssen[1], Jörg Rickli[1,2], April N. Abbott[3], Michael J. Ellwood[4], Benjamin S. Twining[5], Daniel C. Ohnemus[6], Philipp Nasemann[1], Delphine Gilliard[1], Samuel L. Jaccard[1,7]

[1]University of Bern Institute of Geological Sciences & Oeschger Center for Climate Change Research, Baltzerstrasse 1-3, 3012 Bern, Switzerland. Emails: david.janssen@geo.unibe.ch; philipp.nasemann@geo.unibe.ch; delphine.gilliard@students.unibe.ch
[2]Institute of Geochemistry and Petrology, ETH Zürich, Zürich, Switzerland. Email: joerg.rickli@erdw.ethz.ch
[3]Department of Earth & Environmental Sciences, Macquarie University, Sydney NSW, Australia. Email: abbot152@d.umn.edu
[4]Research School of Earth Sciences, Australian National University, Canberra, Australia. Email: michael.ellwood@anu.edu.au
[5]Bigelow Laboratory for Ocean Sciences, East Boothbay, ME, USA. Email: btwining@bigelow.org
[6]University of Georgia, Skidaway Inst. of Oceanography, Dept. of Marine Sciences, Savannah GA, USA; Email: dan@uga.edu
[7]University of Lausanne Institute of Earth Sciences, Lausanne, Switzerland. Email: Samuel.Jaccard@unil.ch

Keywords: chromium, chromium isotopes, GEOTRACES, paleoproxy, biogeochemical cycling, benthic flux

Highlights:

- Cr release from biogenic particles is not coupled to C respiration or N & P release
- Release of biogenic Cr follows the enrichment factor from the global δ^{53}Cr–Cr array
- Benthic Cr flux is seawater-derived and is a major source locally, perhaps globally
- A deep regeneration cycle and circulation explain global Cr, δ^{53}Cr distributions
- Biogenic controls and a diagenetic cycle may complicate Cr paleoproxy applications

Abstract

Chromium (Cr) has shown promise as a paleoceanographic proxy due to the redox-driven control of dissolved Cr concentrations ([Cr]) and stable isotope composition ($\delta^{53}Cr$). However, substantial uncertainties in the biogeochemical Cr cycle have limited its paleoproxy application to date. To improve the mechanistic understanding of Cr cycling in the modern ocean and strengthen its potential proxy applications, we present new data from regeneration incubations, bottom and sediment pore waters, and a compilation of intermediate and deep water data. While Cr removal and biological export from the surface ocean is associated with organic carbon export, the deep water release of dissolved Cr from sinking particles is not directly dependent on organic carbon respiration, as indicated by differing trends between Cr, oxygen utilization and the regeneration of organic-associated macronutrients (e.g. N, P). Pore water and bottom water data demonstrate that benthic Cr fluxes are locally important and may be significant globally. The pore water dissolved Cr flux at our $CaCO_3$-rich site is likely driven by the re-release of Cr scavenged from the water column by sinking particles, with minor contributions from lithogenic phases. We argue this is consistent with the highest open ocean [Cr] to date being found in the water column below oxygen minimum zones, likely reflecting the release of scavenged Cr in deep waters or surface sediments. Chromium released from suspended particles and surface sediments follows the global $\delta^{53}Cr$–[Cr] array, supporting the proposed role of biological export and regeneration in shaping global Cr and $\delta^{53}Cr$ distributions. Global intermediate and deep water [Cr], $\delta^{53}Cr$ and Cr:macronutrient relationships are thus shaped by a synergy of circulation patterns, water mass mixing, a deep Cr regeneration cycle, and benthic Cr sources. A biogenic control on global Cr distributions indicates that sedimentary Cr records may reflect biogenic as well as O_2-dependent processes, while more research is needed to assess sediment Cr record fidelity based on an active diagenetic cycle.

1. Introduction

Oceanic distributions of dissolved Cr show nutrient-type behavior, generally resembling the primary macro- and micronutrients, though with muted surface depletions and enrichments at depth (e.g. Campbell & Yeats, 1981; Jeandel et al., 1987). Thermodynamic calculations predict that oxidized Cr(VI), a soluble oxyanion with low particle reactivity (Semeniuk et al., 2016), should account for all dissolved Cr in the oxygenated ocean (Elderfield et al., 1970). However, the reduced form, Cr(III), is regularly found at low levels in oxygenated seawater ($\leq$ ~15% of total dissolved Cr, e.g. Cranston & Murray, 1978; Cranston, 1983; Jeandel & Minster, 1987; Achterberg & van den Berg, 1997; Connelly et al., 2006; Janssen et al., 2020), and may constitute a major fraction of dissolved Cr in oxygen minimum zones (OMZs; e.g. Murray et al., 1983; Rue et al., 1997). Chromium(III) is relatively insoluble and readily adsorbs to mineral and organic surfaces (e.g. Cranston & Murray, 1978; Mayer et al., 1984). Therefore redox transformations likely play a central role in Cr biogeochemical cycling. Iron(II) is an important Cr(VI) reductant in natural aquatic systems (Pettine et al., 1998), and Mn oxides are a primary Cr(III) oxidant (van der Weijden & Reith, 1982; Milletto et al., 2021), especially in Mn-rich environments such as sediments (Oze et al., 2007).

The primary dissolved Cr removal processes in the ocean, both involving Cr reduction followed by particle scavenging, are removal in OMZs and biologically-mediated export (e.g. Scheiderich et al., 2015). Chromium removal in OMZs has been reported in the eastern tropical North Pacific (ETNP) (Murray et al., 1983; Rue et al., 1997; Moos et al., 2020) and the eastern tropical South Pacific (ETSP) (Nasemann et al., 2020), but this process may be more efficacious in anoxic shelf environments (cf. Moos et al., 2020; Nasemann et al., 2020). Correlations between Cr and particulate organic carbon in sinking particles (Connelly et al., 2006), Cr(III) adsorption onto marine phytoplankton (Semeniuk et al., 2016), and agreements between dissolved Cr deficits and productivity-based inferred removal (Janssen et al., 2020) support a Cr sink associated with biological export. However, the subtle gradients in [Cr] depth profiles suggest that release from biogenic particles is relatively minor (e.g. Scheiderich et al., 2015; Goring-Harford et al., 2018; Moos & Boyle, 2019; Rickli et al., 2019) meaning the contribution of biogenic Cr fluxes to concentrations in the ocean interior may be limited, and circulation may play an important role in

shaping distributions (Connelly et al., 2006; Scheiderich et al., 2015; Goring-Harford et al., 2018; Rickli et al., 2019). Elevated bottom water [Cr] suggests surface to deep [Cr] gradients may be influenced by a flux from marine sediments (Murray et al., 1983; Jeandel and Minster, 1987; Achterberg & van den Berg, 1997) consistent with shallow pore water Cr enrichments on the California shelf due to release from organic matter (Shaw et al., 1990).

Chromium redox transformations are accompanied by isotopic fractionation. While fractionation patterns during Cr oxidation are variable (see discussion in Zink et al., 2010; Milletto et al., 2021), reduction consistently enriches light isotopes in Cr(III) (e.g. Wanner & Sonnenthal, 2013). The redox control on [Cr] and δ^{53}Cr makes δ^{53}Cr a potentially powerful tracer of paleoredox conditions, especially in early earth studies (e.g. Frei et al., 2009). However, application and interpretation of δ^{53}Cr records require an accurate and mechanistic understanding of the process(es) that control Cr budgets and isotopic fractionation in terrestrial environments, the global ocean, and during incorporation of Cr into sediment records. The systematic relationship between seawater [Cr] and δ^{53}Cr suggests that redox transformations likely control the global distribution of oceanic δ^{53}Cr (Scheiderich et al., 2015; Goring-Harford et al., 2018; Moos et al., 2019; Rickli et al., 2019; Janssen et al., 2020; Moos et al., 2020; Nasemann et al., 2020) implying an effective isotope enrichment factor (ε) of approximately -0.7 ‰ associated with Cr reduction and removal. Recent δ^{53}Cr and [Cr] data demonstrate fractionation associated with biologically driven Cr removal in the open ocean (Janssen et al., 2020). Similarly, Cr removal in shelf settings (Goring-Harford et al., 2018), as well as in OMZs (Moos et al., 2020; Nasemann et al., 2020) can result in isotopic fractionation. However, isotope fractionation factors for these removal processes remain poorly constrained.

To address uncertainties in the modern ocean Cr budget and the role of biogenic processes in seawater δ^{53}Cr distributions, we present dissolved [Cr], δ^{53}Cr and [Cr(III)] from shipboard incubations, new intermediate and deep water [Cr] and δ^{53}Cr data from eight research expeditions in the Southern, Pacific and Atlantic Oceans, and pore water [Cr] data from the Tasman Sea.

2. Oceanographic background - Formation of intermediate and deep waters in the Southern Ocean and advection into the Pacific and Atlantic Oceans

The Southern Ocean is the formation site for much of the global deep and intermediate waters, including Antarctic Intermediate Water (AAIW) and Upper and Lower Circumpolar Deep Water (U/L-CDW). The extent to which these intermediate and deep waters penetrate into lower latitudes in the Pacific and Atlantic Oceans varies depending on formation sites, bathymetry, and the prevalence of other water masses.

AAIW is reflected in salinity minima in depth profiles, although this erodes with northward transport, and it is found at neutral densities ~27 < γ^n < ~27.4 (Orsi et al., 1995; Sloyan & Rintoul, 2001; Talley et al., 2011; Bostock et al., 2013). AAIW flows northward to the tropical South Pacific (~10-15° S) where it mixes with Equatorial Pacific Intermediate Water, itself derived from the mixing of AAIW and Pacific Deep Water (PDW) (Bostock et al., 2013). Atlantic AAIW is diluted by mixing during northward transport, as evidenced by increased salinity, and reaches a maximum extent slightly beyond the equator (Suga & Taley, 1995). Tropical Atlantic AAIW is found at a depth of around 700-800 m dicernible by low salinity (~34.20-34.40) and high O_2 (≥ 190 μmol kg^{-1}) south of 20° S. Basin-scale circulation patterns result in more O_2-depleted AAIW north of 20° S impacted by organic matter respiration and vertical mixing (Suga & Talley, 1995).

The deep waters of the Pacific Ocean comprise UCDW, LCDW and PDW, the latter of which is largely found at similar densities as UCDW (γ^n < 28.0; T > 1.5° C; S < 34.65 PSU) and is formed as the colder, more saline and more oxygen rich LCDW (γ^n > 28.0) is upwelled and mixed throughout Pacific (e.g. Orsi et al. 1995; Sloyan & Rintoul, 2001; Kawabe & Fujio, 2010; Talley et al. 2011). Densities occupied by UCDW transition to predominantly PDW in the tropical South to subtropical North Pacific, with UCDW reaching further north in the western Pacific. LCDW extends into the North Pacific along the western side

of the basin, and the northernmost reaches are characterized by elevated [$Si(OH)_4$] (≥170 μmol kg^{-1}) (Kawabe & Fujio, 2010). CDW enters the South Atlantic below AAIW and can be dominant as far north as ~25° S, but the relative contribution of CDW weakens as the water mass continues northward with CDW accounting for ≤ 50% of deep waters in the tropical Atlantic (Larqué et al., 1997).

3. Methods

Intermediate and deep water [Cr] and $\delta^{53}Cr$ samples were collected on RV *Investigator* expeditions IN2018_V02 (Mar-2018) and IN2018_V04 (Sept-Oct 2018), ACE Legs 1 (Dec-2016 to Jan-2017) and 2 (Jan-2017 to Feb-2017), GEOTRACES section GP13 (Australian leg, May-June 2011), RV *Meteor* cruise M77/4 (Jan-Feb 2009), Line P cruise 2012-13 (Aug-2012), and RV *Discovery* cruise DY110 (Oct-Nov 2019) (Figure 1). Further analyses were performed on bottom and pore waters (IN2018V_04) and on samples from shipboard regeneration incubation experiments (IN2018V_02).

3.1 New and literature data from the Southern, Pacific and Atlantic Oceans

We present a compilation of new and literature [Cr] data in Southern-sourced intermediate and deep waters across the Southern, Pacific, and Atlantic Oceans (Figure 1). Literature [Cr] data were not included if: (1) hydrographical data (temperature, salinity) are missing, (2) the data have not been peer-reviewed, or (3) later publications identified them as suspect or incorrect.

We add 12 samples from the Indian Sector of the Southern Ocean (ACE Leg 1) and one sample from the Drake Passage (ACE Leg 2) to [Cr] and $\delta^{53}Cr$ available from the Pacific Sector of the Southern Ocean (Rickli et al., 2019) to further constrain the composition of southern-sourced end-members. The Drake Passage sample constrains the characteristics of intermediate waters entering the Atlantic Ocean.

We present data from five stations in the subantarctic Southern Ocean and the Tasman Sea (IN2018V_02 and IN2018V_04, 26 samples) and four stations in the Tasman Sea and subtropical South Pacific (GEOTRACES section GP13, 12 samples) in order to characterize waters advecting northward into the Pacific Ocean.

Four new samples from one of the most intense OMZs in the global ocean (ETSP near Peru; M77/4) are added to existing ETSP (Nasemann et al., 2020), ETNP OMZ (Murray et al., 1983; Rue et al., 1997), and subtropical North Pacific (Moos & Boyle, 2019) data. Additionally, we present four new samples from a profile in the subarctic North Pacific (Line P 2012-13) to characterize the northern extent of deep water in the Pacific Ocean. Previous subarctic North Pacific literature data for [Cr] in PDW and LCDW (Cranston, 1983; Mugo & Orians, 1993) show a clear offset from recent high-precision data and are not used (see Table S11).

To follow the northward advection of AAIW into the equatorial Atlantic, we present seven samples from five stations along a meridional transect (DY110). Additional literature data from the Atlantic are limited, with only one sample within AAIW (station 11.5, Goring-Harford et al., 2018) and no available CDW data.

3.2 Water column dissolved Cr sampling

IN2018_V02, IN2018_V04, and GP13 samples were collected using an autonomous trace metal clean rosette system and gravity filtered through acid-cleaned 0.2 µm filters (Pall Acropak) into acid cleaned LDPE bottles in a class 100 clean van. IN2018 samples were acidified to pH < 2 (2 mL L^{-1} sub-boiling distilled concentrated HCl) on land and stored for 3-26 months before analysis. GP13 samples were stored frozen until 2019, at which point they were thawed, acidified as for IN2018 samples, and stored at least 7 months before analysis. DY110 samples were collected with a conventional CTD-rosette, gravity filtered through acid-cleaned 0.2 µm filters (Pall Acropak) acidified to pH ≈ 2 (1 mL L^{-1} concentrated HCl), and

stored for at least 3 months before analysis. Sampling and sample handling are discussed in detail elsewhere for ACE (Rickli et al., 2019), M77/4 (Nasemann et al., 2020) and Line P (Janssen & Cullen, 2015).

3.3 Incubation design and sampling

Incubation regeneration experiments were carried out in the subantarctic Southern Ocean south of Tasmania (IN2018_V02) in acid-cleaned 20 L LDPE cubitainers with Teflon-lined caps. Three regeneration experiments were conducted, with differences in incubation temperature and the particle collection depth (supplemental material). Each experiment consisted of two treatments, each in triplicate. Cubitainers were filled with filtered (0.2 µm) surface (~5 m) seawater collected using a trace metal-clean tow fish, and aliquots were collected for initial (T_0) nutrients, [Cr] and δ^{53}Cr before particle inoculation. Filled cubitainers were stored in the dark at 1° C until inoculating with particles (within 8 hours of filling). Ambient suspended particle samples from the oxic water column were collected onto acid-cleaned 1 µm polycarbonate filters using in-situ pumps (McLane). Particles were resuspended from these filters, forming a particle-rich slurry that was added to the individual cubitainers to result in particulate concentrations approximately 2-4 fold above natural levels. Because only resuspended particles were added to the incubaitons, the high Cr blanks associated with many filter materials (e.g. Scheiderich et al., 2015) will not impact the incubations.

Particle-inoculated cubitainers were incubated in the dark at either 4° C (ambient) or 1° C (cold treatment) for five days, with three subsampling time points. For subsampling, the cubitainers were transported to a Class 100 clean van, gently mixed, and subsampled into acid-cleaned LDPE bottles (for trace metals) or polycarbonate tubes (for macronutrients). Subsamples for trace metals were transported to a laminar flow hood and filtered through acid-cleaned 0.4 µm polycarbonate filters using a Teflon vacuum filtration apparatus (Savillex). Loss of Cr to container walls has been shown to be minimal over short timeframes (e.g. Semeniuk et al., 2016) and was not considered here. Chemically-labile particulate metal and P concentrations were determined with magnetic-sector ICPMS following solubilisation with a heated mixture of reductant (hydroxylamine hydrochloride) and weak acid (acetic acid) designed to dissolve

biogenic material and Mn and Fe oxides (Berger et al. 2008). Analytical procedures followed those previously described in Rauschenberg and Twining (2015).

3.4 Bottom water, pore water and sediment sampling

Pore water and bottom water samples for this study were collected from a multicore deployment near Station PS3 in the Tasman Sea (Figure 1, 3349 m water depth). Cores for pore water, bottom water, and sediment samples were processed in an N_2 environment. A bottom water sample was extracted from the core tube approximately 10 cm above the sediment-water interface using an acid-cleaned rubber-free syringe and filtering through a 0.45 µm syringe filter into an acid-cleaned LDPE bottle. The bottom water was visibly clear and free from sediment resuspension, and the sediment surface appeared undisturbed.

Pore water samples were collected following procedures outlined in Abbott et al. (2015). In brief, 1 cm depth intervals were placed into acid-cleaned centrifuge tubes in a glove bag, sealed, then centrifuged at 4500 rpm for 20 minutes. The pore water (supernatant) was extracted from centrifuged samples and filtered as outlined for bottom water. The samples were acidified, stored and analyzed for [Cr] by isotope dilution as described in section 3.6. Centrifuged sediments were stored frozen until freeze-dried, then analyzed for bulk composition ($CaCO_3$, organic matter, lithogenic material; supplemental material).

3.5 Cr(III) samples

Dissolved chromium redox speciation (Cr(III)) samples were processed at sea using magnesium hydroxide ($Mg(OH)_2$) co-precipitation, then analysed by isotope dilution ICP-MS on land at the University of Bern following the procedures of Janssen et al. (2020) (external [Cr(III)] 1σ = 10% RSD, Janssen et al., 2020).

3.6 Chromium concentrations and $\delta^{53}Cr$

Procedures for the determination of total dissolved Cr concentrations ([Cr]) and stable isotope composition ($\delta^{53}Cr$) are described in detail in Rickli et al. (2019), with minor modifications (see supplemental material;

239 Janssen et al., 2020; Nasemann et al., 2020). Briefly, preliminary [Cr] for spiking purposes (not reported)
240 was determined by isotope dilution on small sample aliquots by $Mg(OH)_2$ co-precipitation followed by
241 cation exchange chromatography. The final reported [Cr] is from $\delta^{53}Cr$ determinations, except when $\delta^{53}Cr$
242 samples were not available (pore waters and incubation intermediate time points). Pore water samples (0.2
243 mL) were dried rather than co-precipitated before chromatography. For $\delta^{53}Cr$, a 0.25-1 L sample aliquot
244 was spiked with ^{50}Cr-^{54}Cr double spike, pre-concentrated by $Mg(OH)_2$ co-precipitation, and purified by a 2
245 step column chromatography.
246
247 Samples were analyzed on a ThermoFisher Neptune Plus MC-ICP-MS at the University of Bern following
248 Rickli et al. (2019). $\delta^{53}Cr$ procedural blanks were 0.3-0.6 ng Cr and insignificant relative to sample Cr.
249 $\delta^{53}Cr$ data are reported relative to the NIST SRM 979. Internal uncertainties were generally 0.02-0.03 ‰
250 (2 SEM); external reproducibility, based on replicate analyses of seawater samples, is ± 0.033 (2 SD) for
251 $\delta^{53}Cr$ and <1% (1 RSD) for [Cr] (see Janssen et al., 2020). In addition to the zero reference NIST SRM 979,
252 a Merck Cr(III) standard was run to monitor accuracy ($\delta^{53}Cr$ = -0.426 ± 0.027 ‰, n = 9; literature: $\delta^{53}Cr$ =
253 -0.443 ± 0.022 ‰, Schoenberg et al., 2008). The procedural accuracy of our method has been validated by
254 an inter-laboratory comparison (Rickli et al., 2019).
255
256 **4. Results and Discussion**
257
258 *4.1 Regeneration incubation experiments*
259 Three incubation experiments to probe for broad, differential effects on the regeneration of trace elements
260 were conducted at the same location in the subantarctic Southern Ocean (Figure 1) within 10 days of each
261 other, with varying experimental design (collection depth and incubation temperatures) and natural
262 variability in the initial particulate regime and elemental concentrations. Only one incubation (Inc. 3)
263 generated significant differences in [Cr] and $\delta^{53}Cr$ by the final time point. We focus on this incubation here,
264 with results from Inc. 1 and 2 provided in the supplemental material (Section S1, Figures S1, Tables S3-

S4). Initial particulate P (pP), Mn (pMn) and Fe (pFe) from all three incubations are shown in Table S1. Flowcam imaging data indicate that particles in all three incubations were small (mostly ~2 µm, nearly all < 6 µm), with a high abundance of flagellates (data not shown), while regional dust deposition is very low (Mahowald et al., 2005), confirming a predominantly biogenic particulate composition.

There was minimal to no net regeneration of organic-associated macronutrients as indicated by the lack of macronutrient variability (N and P) (Figure 2, Table S2). Chromium concentrations, [Cr(III)] and $\delta^{53}Cr$ remained stable over the first three days of the treatments. However, [Cr] increased by an average of 0.46 ± 0.14 and 0.56 ± 0.18 nmol kg^{-1} (1 SD of the triplicates) by the final sampling for the ambient and cold treatments, respectively (Figure 2), demonstrating that Cr release was independent from organic carbon respiration. Small increases in [Cr(III)] were also observed by the end of the incubation, though the increases in [Cr] were approximately seven times larger. Particulate Cr was probably primarily Cr(III) – Cr(III) dominates the Cr adsorbed to biogenic particles (e.g. Semeniuk et al., 2016) and the Cr content of calcium carbonate, hosting Cr(VI), is very low (Remmelzwaal et al., 2019). Therefore, due to the small changes in [Cr(III)], particulate Cr was either oxidatively released or rapidly oxidized after release.

Particulate Mn oxides are known to oxidize Cr(III), facilitating particulate Cr(III) dissolution (Oze et al., 2007), and incubated particles were enriched in Mn beyond typical cellular quotas (Table S1, Twining & Baines, 2013), indicating the presence of Mn oxides. Therefore, Cr oxidation coupled to the reduction of Mn oxides could explain dissolved Cr release without N and P regeneration or increases in [Cr(III)]. Indeed, the timing of the release of Cr in Inc. 3 matches a decrease in pMn (Figure 2). Differences between the three incubations can also be explained by Mn oxides. Incubations from 150 m had much higher pMn than those from shallower depths (Inc. 1, 100 m & Inc. 2; Table S1), following trends in oceanic pMn distributions (Ohnemus et al., 2019), and explaining the lack of Cr release in shallower treatments. Particulate Fe in Inc. 1 was higher than in Inc. 3 (Table S1), indicating more Fe-rich mixed oxides, which may impact Cr oxidation and explain differences between these incubations. The enriched incubation

particle concentrations, possibly in combination with the formation of particle aggregates, would help to increase the probability of oxidative Cr release by particulate Mn oxides relative to ambient seawater conditions. Consequently, oxidative particulate Cr release driven by reduction with Mn oxides would be less likely in natural seawater, suggesting a deeper regeneration cycle for Cr than organic matter respiration influenced by more Mn-rich deeper particles (Ohnemus et al., 2019) and marine sediments.

The increase in [Cr] was accompanied by a statistically significant decrease in δ^{53}Cr in four of six samples (Figure 2, Table S2). δ^{53}Cr decreases were not significant for the remaining two samples, which is consistent with the small increase in [Cr] insufficient to significantly lower δ^{53}Cr. Inter-replicate variability is likely controlled by small initial differences in biological communities and particle compositions in each cubitainer, hence real natural variability, rather than analytical uncertainty, given differences in [Cr] between triplicates were well outside of analytical uncertainty (Figure 2, Table S2). This release of low δ^{53}Cr from particles provides evidence for predictions that Cr adsorbed onto biogenic particles is isotopically light (Scheiderich et al., 2015; Semeniuk et al., 2016; Janssen et al., 2020).

A strong linear relationship is observed between δ^{53}Cr and ln[Cr] in the regeneration incubation samples (r^2 = 0.89) with an implied enrichment factor (ε) = -0.66 ‰. This enrichment factor matches the global δ^{53}Cr–[Cr] array (global $\varepsilon \approx$ -0.70 ‰), and the data plot along the global array (Figure 2). This supports release from biogenic particles as an important process in driving global [Cr] and δ^{53}Cr distributions. While proposed earlier (Scheiderich et al., 2015), previous studies have highlighted that biogenic Cr accumulation was lacking strong support in oceanic depth profiles (Scheiderich et al., 2015; Goring-Harford et al., 2018; Moos & Boyle, 2019; Rickli et al., 2019). This study provides the first direct evidence that Cr release from biogenic particles acts as a control on δ^{53}Cr across intermediate and deep waters, and ultimately also supports the inverse of this process – the adsorption of Cr onto biogenic particles in the surface ocean – as a control of δ^{53}Cr and [Cr] (Scheiderich et al., 2015; Semeniuk et al., 2016; Goring-Harford et al., 2018; Janssen et al., 2020).

317

318 *4.2 Benthic Cr supply: the flux of Cr to bottom waters from pore waters*

319 Pore waters were sampled from calcareous sediments (~3350 m water depth) collected from a shallower
320 feature punctuating the abyssal plain (~4000 to 5000 m) in the Tasman Basin (Figure 1). Regional
321 sedimentation rates are on the order of 1-2 cm kyr^{-1} (Cochran & Osmond, 1976). Organic matter is around
322 1% at the sediment surface, though upper sediments remain oxic and organic carbon content decreases with
323 depth (Table 1, Table S7). Surface sediment Mn/Al (~0.016) and Fe/Al (~0.53) are higher than upper
324 continental crust values (0.009 and 0.48 respectively, Rudnick & Gao, 2003; Table S7), suggesting slight
325 authigenic oxide enrichment, though Fe-Mn oxides are not a dominant phase. Sediment Mn/Al begins to
326 decrease below 11 cm, suggesting oxic conditions in the upper 10 cm and more reducing conditions below
327 this depth.

328

329 Pore water dissolved [Cr] shows a shallow sub-surface maximum (0-1 cm below the sea floor) of 47.4 nmol
330 kg^{-1}, approximately an order of magnitude greater than local bottom waters (4.81 nmol kg^{-1}, Figure 3), and
331 pore water [Cr] generally decreases exponentially with depth. The lowest pore water concentrations are
332 observed in the deepest samples (6.7 nmol kg^{-1} at 9-10 cm depth), which remain elevated relative to bottom
333 water. This upper pore water Cr maximum is consistent with observations by Shaw et al. (1990). In contrast
334 to our observations of maximum pore water [Cr] at the sediment surface, Shaw et al. (1990) observed Cr
335 removal in the uppermost oxic sediments, above the near-surface pore water [Cr] maximum. The absence
336 of Cr removal in our uppermost oxic sediments may reflect the strong differences in bulk sediment
337 composition between the lithogenic-dominated sites in Shaw et al. (1990) and our carbonate-dominated
338 site.

339

340 A near-surface pore water maximum in [Cr] suggests pore waters may act as a diffusive source of dissolved
341 Cr to the ocean. Bottom waters composed of CDW are enriched in dissolved Cr and are isotopically distinct
342 ([Cr] = 4.81 nmol kg^{-1}, $\delta^{53}Cr = 0.76 \pm 0.03$ ‰) from CDW at nearby stations not in contact with sediments

([Cr] = 3.95 nmol kg^{-1}, $\delta^{53}Cr$ = 0.84 ± 0.03 ‰, 2SD, n = 6 samples ≥ 3000 m at stations TS8 and PS2, Table S9). Given the gradient of [Cr] from the pore water to the overlying bottom water, the diffusive flux of dissolved Cr can be estimated using Equation 1

$$Flux_{Cr} = D_s \frac{\Delta C}{\Delta z} \quad \text{Equation 1}$$

where D_s is the Cr diffusion coefficient corrected for temperature and tortuosity (supplemental material, see also Abbott et al., 2015), giving an estimated benthic flux of ~3.2 nmol Cr cm^{-2} yr^{-1}.

To contextualize this, if global oxic sediments were characterized by a benthic source of similar magnitude to that observed at our site, the global benthic Cr flux would be comparable to or larger than riverine inputs, currently believed to be the dominate Cr source (Bonnand et al., 2013; supplemental material), consistent with box model estimates (Jeandel & Minster, 1987). While quantitative estimates of global benthic Cr fluxes await greater data availability across diverse sediment types, our data identify that benthic sources are at least locally important and support previous studies that: (1) have argued for benthic Cr fluxes based on globally distributed elevated deep water [Cr] (Cranston, 1983; Murray et al., 1983; Jeandel & Minster, 1987), and (2) have invoked elevated pore water [Cr] to explain Cr enrichments in planktonic foraminifera in sediments compared to water column samples (Remmelzwaal et al., 2019).

We use the bulk sediment composition to examine potential sources of Cr to pore waters by applying mass balance calculations based on the average composition of the upper 4 cm, reported Cr concentrations of these phases, and regional sedimentation rates (Table 1). These calculations suggest that neither lithogenic nor carbonate-hosted Cr can account for the Cr flux out of these carbonate-rich and detrital-poor sediments. Nor is the Cr content of surface phytoplankton (~1-21 ppm, Martin & Knauer, 1973) high enough to explain observations (Table 1). Therefore, we suggest a combination of mechanisms causing Cr enrichments in particles delivered to sediments can explain the observed pore water data. First, respiration may result in a relative Cr enrichment in particles reaching the seafloor because the release of Cr from particles appears

decoupled from organic matter respiration (see sections 4.1, 4.3). At the same time, scavenging of particle-reactive Cr(III) may increase the Cr content on biogenic and non-biogenic particles. Regardless of which process(es) are involved, the Cr released from these sediments must largely be derived from the water column based on mass balance and is incorporated into the sediments as particle-adsorbed Cr that has been scavenged onto particle surfaces in the upper ocean (Connelly et al., 2006; Semeniuk et al., 2016; Janssen et al., 2020), and at intermediate depths (see section 4.3), while detrital Cr may be more inert. Mn oxides in surface sediments may also facilitate oxidative release of Cr(III) coupled to Mn reduction.

To better constrain the origin of dissolved Cr in pore water we calculate its $\delta^{53}Cr$ from mass balance, using observed bottom and deep water [Cr] and $\delta^{53}Cr$ (bottom water: [Cr] = 4.81 nmol kg^{-1}, $\delta^{53}Cr = 0.76 \pm 0.03$ ‰; deep water: ([Cr] = 3.95 nmol kg^{-1}, $\delta^{53}Cr = 0.84 \pm 0.03$ ‰, 2SD; supplemental material). Pore water $\delta^{53}Cr$ is estimated at 0.34 ± 0.25 ‰ (2 SEM propagated error), which is heavier than silicate earth (-0.124 ± 0.101 ‰, Schoenberg et al., 2008). While the closeness of these ranges indicates that some lithogenic component may contribute to the pore water flux, mass balance calculations, combined with the likely refractory nature of lithogenic Cr (e.g. Bauer et al., 2019), indicate that it is unlikely that lithogenic Cr contributes significantly to the pore water flux. In contrast, pore water $\delta^{53}Cr$ is lighter than dissolved $\delta^{53}Cr$ in the upper 1000 m ($\delta^{53}Cr \approx 1.1$-$0.9$ ‰) by a similar amount as the enrichment factor predicted by the global $\delta^{53}Cr$–[Cr] array ($\varepsilon \approx -0.7$ ‰). In other words, removal of dissolved Cr to particles in the upper 1000 m with an enrichment factor following the global array would result in $\delta^{53}Cr_{particulate}$ similar to the calculated $\delta^{53}Cr_{pore\ water}$.

Although the exact origin of pore water Cr is hard to discern and may include biogenic, scavenged, and lithogenic sediment components, our mass balance calculations highlight the importance of internal processes acting to redistribute Cr within the water column, transferring dissolved Cr from upper waters to deep waters. Therefore, the benthic flux may act more as an attenuation of the Cr sink term associated with particle export than an entirely new Cr source. Pore water data from diverse sediment types are needed to

394 determine whether a truly new contribution from lithogenic material may be regionally important in more
395 lithogenic-rich sediments.
396
397 *4.3 Accumulation of Cr in intermediate and deep water masses*
398 To investigate the implications of the mechanistic insight from our incubation and pore water findings on
399 the global ocean, a compilation of globally-distributed [Cr] data is presented along with macronutrients and
400 apparent oxygen utilization (AOU, a quantification of the O_2 used for organic matter respiration) following
401 the northward advection of water masses originating in the Southern Ocean (Figure 4). Intermediate and
402 deep waters are split into three water mass ranges based on hydrographic properties: AAIW, UCDW/PDW
403 and LCDW (Figure S2, Tables S9-S10).
404
405 Deeper water masses (UCDW and LCDW) show relatively uniform [Cr], AOU and macronutrients at their
406 southern origin, and concentrations increase with northward transport (Figure 4). However, key differences
407 emerge between tracers primarily reflecting the respiration of organic matter (AOU, PO_4), phytoplankton
408 frustule-associated $Si(OH)_4$, and [Cr]. AOU and PO_4 consistently show latitudinal maxima in the upper
409 deep water mass (UCDP/PDW) relative to LCDW, in agreement with global distributions of PO_4, NO_3 and
410 O_2 throughout the ocean (e.g. Schlitzer et al., 2018). Similar behaviour of Cr results in broadly correlated
411 Cr–AOU and Cr–PO_4 distributions (Figure 5), where correlations weaken as [Cr] increases. However,
412 $Si(OH)_4$ shows maxima in LCDW, and [Cr] in LCDW is comparable to or higher than in UCDW. These
413 deeper maxima, reflecting an apparent deeper regeneration cycle, may reflect globally important benthic
414 sources as has been shown for Si (Treguer & de la Rocha, 2013), consistent with our calculated pore water
415 fluxes and earlier global Cr cycle models (Jeandel & Minster, 1987). Chromium–$Si(OH)_4$ distributions
416 show a stronger correlation ($r^2 = 0.58$, n = 65) than Cr–AOU ($r^2 = 0.44$, n = 71) and Cr–PO_4 ($r^2 = 0.52$, n =
417 67) (Figure 5), supporting Cr release from biogenic material as being mechanistically independent from
418 organic matter respiration.
419

The absolute maxima in deep water [Cr] are found below the ETSP OMZ, where accumulated Cr represents up to ~45% of total deep water [Cr] based on Southern Ocean end members. While suboxic sediments are a net sink term (e.g. Moos et al., 2020; Nasemann et al., 2020), these deep water [Cr] enrichments may reflect the proximity to a benthic source from deeper oxic sediments (section 4.2, see also Figure 1). Deep ETNP samples are also enriched relative to the subtropical South Pacific and subarctic North Pacific (Figure 4), suggesting a connection to the intense OMZs overlying these deep [Cr] enrichments (Murray et al., 1983; Rue et al., 1997; Moos et al., 2020). Mechanistically, the enhanced export of particulate Cr to depth from water column removal combined with the elevated Mn present below these OMZs (e.g. Murray et al., 1983) would facilitate the oxidative release of Cr from particles in the water column or from oxic pore waters. This Cr-specific enrichment process would cause deep waters below intense OMZs to deviate from correlations between Cr and macronutrients, which is confirmed by the resulting strengthening of the Cr correlation with Si ($r^2 = 0.73$) when removing samples below the ETSP OMZ (correlations with PO_4 ($r^2 = 0.56$) and AOU ($r^2 = 0.41$) remain similar; Figure 5).

Intermediate waters are associated with high carbon respiration with northward advection (Figure 4). Southern waters with properties similar to newly-formed AAIW show the highest [Cr], and concentrations are generally stable or decrease with northward transport, indicating [Cr] is decoupled from organic matter respiration. A general decrease in [Cr] northward is found for Atlantic AAIW accompanied by increasing salinity ($r^2 = 0.54$). This trend likely reflects mixing of AAIW with Cr-poor but more saline thermocline waters and NADW (Figure 6, Rickli et al. 2019). However, the weakness of the correlation likely suggests more complicated mixing of multiple water masses, variable scavenging of Cr in intermediate waters, or both.

4.3.1 Implications of water mass [Cr] accumulation trends on Cr–macronutrient coupling in the global ocean

Widely observed correlations between [Cr] and macronutrient concentrations suggest shared biogeochemical controls (e.g. Campbell & Yeats, 1981; Cranston, 1983; Jeandel & Minster, 1987; Rickli et al., 2019; Nasemann et al., 2020). Recent studies of other metal–macronutrient associations have highlighted the importance of three dimensional processes, rather than vertical-controlled simplifications, with pre-formed relationships (e.g. Vance et al., 2017), scavenging, and variable metal:macronutrient uptake ratios across taxa and nutrient regimes (Quay et al., 2015; Ohnemus et al., 2019) driving globally-correlated distributions.

While correlations between [Cr] and PO_4 exist on different spatial scales (e.g. Cranston, 1983; Rickli et al., 2019), biogenic Cr fluxes are low relative to other nutrient-type metals and macronutrients as apparent in smaller surface [Cr] depletions, lower surface-to-deep [Cr] gradients, reduced [Cr] accumulation in global deep water, and [Cr] accumulation in subsurface waters that is independent from organic matter respiration (sections 4.1-4.3, Figure 5). This means that the observed associations between [Cr] and PO_4 probably reflect mixing between distinct oceanic end-members (see Rickli et al., 2019) rather than coupled vertically-driven processes (e.g. particle sinking and regeneration). Therefore end-member pre-formed Cr:macronutrient ratios would shape much of the Cr–macronutrient relationships in the ocean interior, while end-members impacted by biological uptake at their formation sites, and water mass-driven Cr:macronutrient associations could result in variable regional relationships.

A prominent benthic source of dissolved Cr provides a mechanistic explanation for [Cr] and $Si(OH)_4$ coupling by vertical processes in addition to water mass mixing. However, deep water data demonstrate that [Cr] and $Si(OH)_4$ can decouple (Figures 4-5), and local differences in Cr–$Si(OH)_4$ slopes (Jeandel & Minster, 1987) suggest the relationship between Cr and $Si(OH)_4$ may reflect a combination of advection and mixing of waters with different pre-formed Cr:$Si(OH)_4$ ratios, Cr and $Si(OH)_4$ drawdown by phytoplankton in surface waters, and the impact of sediment type and location on benthic dissolved Cr and $Si(OH)_4$ fluxes (e.g. elevated [Cr] below OMZs, Figures 4-5). Based on these variable controls on

Cr:macronutrient ratios, and recognizing that intermediate and deep water circulation likely plays a central role, interpretations of Cr–macronutrient trends within depth profiles should be made with caution.

5. An updated global ocean Cr biogeochemical cycle

The foundations for understanding oceanic $\delta^{53}Cr$ distributions were presented by Scheiderich et al. (2015), who first demonstrated a tight coupling between [Cr] and $\delta^{53}Cr$. Building on the [Cr] literature, Scheiderich et al. (2015) hypothesized that the controls on $\delta^{53}Cr$ were the same as those known for [Cr]: reduction and removal in OMZs and Cr export with biogenic particle flux along with regeneration from biogenic material. Subsequent $\delta^{53}Cr$ research has attempted to assess these mechanisms and their associated fractionations to identify their roles in the global Cr and $\delta^{53}Cr$ cycle. We combine these initial hypotheses and recent advancements with our new data to improve our mechanistic understanding of Cr cycling in the global ocean and highlight remaining uncertainties. This set of mechanistic controls define how internal oceanic processes regulate $\delta^{53}Cr$, forming the global relationship (Figure 7 panel A), and will help to guide paleoceanographic applications of marine $\delta^{53}Cr$.

Here, we have demonstrated that Cr release from biogenic particles, either in the water column or as a benthic flux, can explain the [Cr]-rich side of the array (Figure 7 panels B and C) consistent with previous work on biological uptake shaping the [Cr]-depleted side of the $\delta^{53}Cr$–[Cr] array (Figure 7 Panel B; Goring-Harford et al., 2018; Janssen et al., 2020). In OMZs, dissolved Cr can be scavenged in the water column (Moos et al., 2020) and at the sediment surface (Moos et al., 2020; Nasemann et al., 2020), a process that largely follows the global array (Figure 7 Panel D). Mixing will generally act to homogenize process- and source-induced variability, with the specific effect depending on the signatures of mixing water masses (Figure 7 panel E, see also section S.4 and Figure S3; Rickli et al., 2019; this study). Hydrothermal circulation may also impact [Cr] and $\delta^{53}Cr$ in the modern ocean and paleoceanographic interpretations (Holmden et al., 2016), but remains largely unconstrained at present (Figure 7 panel F).

Coastal environments are more likely to deviate from the global $\delta^{53}Cr$–[Cr] array due to localized influences, including shelf sources (Goring-Harford et al., 2018) (Figure 7 Panel C), more quantitative removal in shelf OMZs (Nasemann et al., 2020, Figure 7 Panel D); dilution from meltwater (Scheiderich et al., 2015, Figure 7 Panel E), and local riverine inputs (Figure 7 Panel F). Consequently, reconstructions of seawater $\delta^{53}Cr$ from coastally-sourced marine sediment records, including continental margins, should be approached with caution as these records are likely not reflective of global ocean conditions for $\delta^{53}Cr$ and/or [Cr].

Taken together, the available body of oceanic data indicate that Cr and $\delta^{53}Cr$ distributions are controlled by biological uptake and scavenging onto sinking particles, with local enhanced reduction and scavenging in OMZs, and regeneration from particles in the water column and/or oxic sediments. These signals are then transported and mixed through ocean circulation. Consequently, $\delta^{53}Cr$ records in marine-origin sediments should reflect the combination of these processes, with both export productivity and OMZ reduction contributing to Cr accumulation in sediments and with temporal $\delta^{53}Cr$ records reflecting modification of these processes over time and with changes in global climate. Therefore, $\delta^{53}Cr$ records are not exclusively reflecting changes in O_2 availability. Additional research is needed to understand early sediment diagenesis, as indicated by elevated pore water [Cr], and the extent to which this may alter sediment Cr signals.

6. Conclusions

Our incubation data provide the first direct evidence of Cr release from biogenic particles and demonstrate that the release of Cr is mechanistically independent from the regeneration of major elements in organic matter (e.g. C, N, P), and may instead be related to oxidative release facilitated by Mn oxides. Our pore water data indicate large benthic Cr fluxes as an important local process, and possibly an important component of the ocean's Cr budget. This benthic flux likely reflects the release of Cr scavenged onto particles in the water column, rather than 'new Cr' from the dissolution of lithogenic material. $\delta^{53}Cr$ data from both bottom waters and incubations identify that release from biogenic particles follows the global

δ^{53}Cr–[Cr] array, demonstrating that Cr release, either in deep waters or surface sediments, can explain the high [Cr] end-member of the global δ^{53}Cr–[Cr] array. Furthermore, our data confirm that biogenic export from the surface ocean and release at depth is important in shaping distributions of both [Cr] and δ^{53}Cr throughout the global ocean. Our compilation provides clear evidence of [Cr] accumulation in deep waters, supporting a deep regeneration cycle for Cr that is decoupled from organic matter respiration and includes a potential benthic source. This regeneration is likely particularly strong below tropical Pacific OMZs where the local [Cr] maxium may result from Cr scavenged in OMZ waters being released in underlying oxic waters and sediments. Intermediate waters show stable or decreasing [Cr], reflecting minimal release from particles and a potential net water column Cr sink via scavenging. Because both [Cr] and δ^{53}Cr are impacted by biological and physical processes, and pore water data indicate active cycling in near-surface seidments, the role of these processes with respect to Cr paleoredox proxy viability should be incorporated into future δ^{53}Cr O_2-reconstruction applications.

Data Availability

Full cruise CTD and macronutrient data for cruises IN2018V_02 and IN2018V_04 are available from CSIRO (https://www.cmar.csiro.au/data/trawler/). Full macronutrient and CTD data from the ACE transect are available from the ACE collection on Zenodo (https://zenodo.org/communities/spi-ace). Full macronutrient and CTD data from the M77/4 cruise are available from the Pangaea repository (https://www.pangaea.de/). Full Line P macronutrient and CTD data are available from the Line P website (http://www.waterproperties.ca/linep/data.php). Shipboard incubation data are available in Tables S1-S4. Pore water data are available in Table S5 and sediment data are available in Table S7. New and literature data used for the isopycnal compilation are available in the supplemental material (Tables S9 and S10). *Editorial note: all new data in this manuscript will also be made available as an open access dataset in the Zenodo repository once a final decision is reached on the manuscript, and the data availability statement will be updated to reflect this. For review purposes, all data are also included here.*

Acknowledgements

We thank the captains, crews, and scientific members of the RV *Investigator* cruises IN2018_V02 and IN2018_V04 as well as the trace metal sampling teams, especially Robin Grun, Pamela Barrett, and Kiefer Forsch, the sediment coring team of Kelly-Anne Lawler, Hannah Kumar, Annabel Payne, and Hannah

Wilson, and Phil Boyd for coordinating and planning trace metal operations on cruise IN2018_V02. The authors wish to thank the CSIRO Marine National Facility (MNF) for its support in the form of sea time on RV Investigator, support personnel, scientific equipment and data management. We thank the captains, crew, and scientific personnel of the additional cruises from which we present new data (ACE Leg 1, GP13, M77/4, Line P 2012-13, DY110) as well as Christel Hassler and Andy Bowie for samples from cruise GP13, Nina Schuback for sampling on cruise DY110, and Martin Frank and Patricia Grasse for samples from cruise M77/4. We thank Julijana Krbanjevic for TC/TIC analysis. We acknowledge Zanna Chase, Barbara Grose, and Pete Strutton for logistical support, Zanna Chase for the use of her centrifuge on voyage IN2018V_04, and Martin Wille for sharing analytical expertise, Neptune support, and for helpful discussions. We thank Tim Conway for providing CTD data for the SAFe station. This manuscript was improved by constructive comments from Lou Derry and two anonymous reviewers. This work was supported by the Swiss National Science Foundation (SNSF grant PP00P2_172915) and by a European Research Council (ERC) Consolidator Grant (SCrIPT grant agreement 819139). Chromium data were obtained on a Neptune MC-ICP-MS acquired with funds from the NCCR PlanetS supported by SNSF grant 51NF40-141881. Maps and some figures were made using Ocean Data View (available at http://odv.awi.de).

Author contributions

DJJ led the design of the study along with SLJ, with assistance from MJE, who organized trace metal sampling operations for ACE Leg 1 & IN2018V_02 and all operations for IN2018V_04, BST & DCO, who designed and conducted the shipboard incubations, and ANA, who planned coring operations and conducted sediment and pore water sampling for cruise IN2018V_04. DJJ conducted seawater sampling, processed, and analyzed samples from ACE Leg 1, IN2018V_02, IN2018V_04, and Line P cruise 2012-13. SLJ conducted sampling for ACE Leg 2. DJJ processed and analyzed samples from DY110 and ACE Leg 2. MJE assisted in seawater sampling for ACE Leg 1, IN2018V_02 and IN2018V_04. BT and DO analyzed particulate samples from IN2018V_04 regeneration experiments. PN processed and analyzed samples from M77/4. DJJ and DG processed and analyzed samples from GP13. DJJ led interpretations and writing, and all authors contributed to the manuscript.

References

Abbott, A.N., Haley, B.A., McManus, J., Reimers, C.E. (2015). The sedimentary flux of dissolved rare earth elements to the ocean. *Geochim. Cosmochim. Act*. **154**, 186-200. doi: 10.1016/j.gca.2015.01.010.

586 Achterberg, E.P. & van den Berg, C.M.G. (1997). Chemical speciation of chromium and nickel in the
587 western Mediterranean. *Deep-Sea Res. II*. **44**, 693–720. doi: 10.1016/S0967-0645(96)00086-0.
588 Bauer, K., Cole, D.B., Asael, D., Francois, R., Calvert, S.E., Poulton, S.W., Planavsky, N.J., Crowe, S.A.
589 (2019). Chromium isotopes in marine hydrothermal sediments. *Chem Geol*. **529**, 119286. doi:
590 10.1016/j.chemgeo.2019.119286.
591 Berger, C.J.M., Lippiatt, S.M., Lawrence, M.G., Bruland, K.W. (2008). Application of a chemical leach
592 technique for estimating labile particulate aluminum, iron, and manganese in the Columbia River
593 plume and coastal waters off Oregon and Washington, *J. Geophys. Res. Oc*. **113**, C00B01. doi:
594 10.1029/2007JC004703.
595 Bonnand P., James R.H., Parkinson I.J., Connelly D.P., Fairchild I.J. (2013). The chromium isotopic
596 composition of seawater and marine sediments. *Earth Planet. Sci. Let*. **382**, 10-20. doi:
597 10.1016/j.epsl.2013.09.001.
598 Bostock, H.C., Sutton, P.J., Williams, M.J.M., Opdyke, B.N. (2013). Reviewing the circulation and mixing
599 of Antarctic Intermediate Water in the South Pacific using evidence from geochemical tracers and
600 Argo float trajectories. *Deep Sea Res. I*. **73**, 84-98. doi: 10.1016/j.dsr.2012.11.007.
601 Campbell, J.A. & Yeats, P.A. (1981). Dissolved chromium in the northwest Atlantic Ocean. *Earth Planet.*
602 *Sci. Lett*. **53**, 427–433. doi: 10.1016/0012-821X(81)90047-9.
603 Cochran, J.K. & Osmond, J.K. (1976). Sedimentation patterns and accumulation rates in the Tasman Basin.
604 *Deep Sea Res*. **23**(3), 193-210. doi: 10.1016/0011-7471(76)91324-3.
605 Connelly, D.P., Statham, P.J., Knap, A.H. (2006) Seasonal changes in speciation of dissolved chromium in
606 the surface Sargasso Sea. *Deep Sea Res. Part I*. **53**, 1975–1988. doi: 10.1016/j.dsr.2006.09.005.
607 Cranston, R.E. (1983) Chromium in Cascadia Basin, northeast Pacific Ocean. *Mar. Chem*. **13**, 109–125.
608 doi: 10.1016/0304-4203(83)90020-8.
609 Cranston, R.E. & Murray, J.W. (1978) Determination of chromium species in natural waters. *Anal. Chim.*
610 *Act*. **99**, 275–282. doi: 10.1016/S0003-2670(01)83568-6.
611 Elderfield, H. (1970) Chromium speciation in sea water. *Earth Planet. Sci. Lett*. **9**, 10–16. doi:
612 10.1016/0012-821X(70)90017-8.
613 Frei R., Gaucher, C., Poulton, S.W., Canfield D.E. (2009) Fluctuations in Precambrian atmospheric
614 oxygenation recorded by chromium isotopes. *Nature*. **461**, 250–254. doi: 10.1038/nature08266.
615 Goring-Harford, H.J., Klar, J.K., Pearce, C.R., Connelly, D.P., Achterberg, E.P., James, R.H. (2018).
616 Behaviour of chromium isotopes in the eastern sub-tropical Atlantic Oxygen Minimum Zone.
617 *Geochim. Cosmochim. Act*. **236**, 41-59. doi: 10.1016/j.gca.2018.03.004.

Holmden, C., Jacobson, A.D., Sageman, B.B., Hurtgen, M.T. (2016). Response of the Cr isotope proxy to Cretaceous Ocean Anoxic Event 2 in a pelagic carbonate succession from the Western Interior Seaway. *Geochim. Cosmochim. Act.* **186**, 277-295. doi: 10.1016/j.gca.2016.04.039.

Jeandel, C. & Minster, J.F. (1987) Chromium behavior in the ocean: global versus regional processes. *Global Biogeochem. Cy*. **1**, 131–154. doi: 10.1029/GB001i002p0013.

Janssen, D.J., Cullen, J.T. (2015). Decoupling of zinc and silicic acid in the subarctic northeast Pacific interior. *Mar. Chem*. **177**, 124-133. doi: 10.1016/j.marchem.2015.03.014.

Janssen, D.J., Rickli J., Quay P.D., White A.E., Nasemann P. and Jaccard S.L. (2020). Biological control of chromium redox and stable isotope composition in the surface ocean. *Glob. Biogeochem. Cy*. **34**. doi: 10.1029/2019GB006397.

Kawabe, M. & Fujio, S. (2010). Pacific ocean circulation based on observation. *J. Oceanogr*. **66**, 389-403. doi: 10.1007/s10872-010-0034-8.

Larqué, L., Maamaatuaiahutapu, K., Garçon, V. (1997). On the intermediate and deep water flows in the South Atlantic Ocean. *J. Geophys. Res. Oc*. **106**(C6), 12425-12440. doi: 10.1029/97JC00629.

Mahowald, N.M., Baker, A.R. Bergametti, G., Brooks, N., Duce, R.A., Jickells, T.D., Kubilay, N., Prospero, J.M., Tegen, I. (2005). Atmospheric global dust cycle and iron inputs to the ocean. *Glob. Biogeochem. Cy*. **19**(4), GB4025. doi: 10.1029/2004GB002402.

Mayer, L.M., Schick, L.L., Chang, C.A. (1984). Incorporation of trivalent chromium into riverine and estuarine colloidal material. *Geochim. Cosmochim. Act*. **48**(9), 1717-1722. doi: 10.1016/0016-7037(84)90027-9.

Milletto, M., Wang, X., Planavsky, N.J., Luther, G.W., Lyons, T.W., Tebo, B.M. (2021). Marine microbial Mn(II) oxidation mediates Cr(III) oxidation and isotope fractionation. *Geochim. Cosmochim. Act*. **297**, 101-119. doi: 10.1016/j.gca.2021.01.008.

Moos, S.B. & Boyle, E.A. (2019). Determination of accurate and precise chromium isotope ratios in seawater samples by MC-ICP-MS illustrated by analysis of SAFe Station in the North Pacific Ocean. *Chem. Geol*. **511**, 481-493. doi: 10.1016/j.chemgeo.2018.07.027.

Moos, S.B., Boyle, E.A., Altabet, M.A., Bourbonnais, A. (2020). Investigating the cycling of chromium in the oxygen deficient waters of the Eastern Tropical North Pacific Ocean and the Santa Barbara Basin using stable isotopes. *Mar. Chem*. **221**, 103756. doi: 10.1016/j.marchem.2020.103756.

Mugo R.K. & Orians K.J. (1993). Seagoing method for the determination of chromium(III) and total chromium in sea water by electron-capture detection gas chromatography. *Anal. Chim. Act*. **271**(1), 1-9. doi: 10.1016/0003-2670(93)80545-V.

Murray, J.W., Spell, B., Paul, B. (1983). The contrasting geochemistry of manganese and chromium in the eastern tropical Pacific Ocean. In: Wong C.S., Boyle E., Bruland K.W., Burton J.D., Goldberg E.D.

(eds) Trace Metals in Sea Water. *NATO Conference Series (IV Marine Sciences)*, **9**. Springer, Boston, MA, p. 643-669. doi: 10.1007/978-1-4757-6864-0_37.

Nasemann, P., Janssen, D.J., Rickli, J., Grasse, P., Franck, M., Jaccard, S.L. (2020). Chromium reduction and associated stable isotope fractionation restricted to anoxic shelf waters in the Peruvian Oxygen Minimum Zone. *Geochim. Cosmochim. Act*. **285**, 207-224. doi: 10.1016/j.gca.2020.06.027.

Ohnemus, D.C., Torrie, R., Twining, B.S. (2019). Exposing the Distributions and Elemental Associations of Scavenged Particulate Phases in the Ocean Using Basin-Scale Multi-Element Data Sets. *Glob. Biogeochem. Cy*. **33**(6), 725-748. doi: 10.1029/2018GB006145.

Orsi, A.H., Whitworth III, T., Nowlin Jr, W.D. (1995). On the meridional extent and fronts of the Antarctic Circumpolar Current. *Deep Sea Res I*. **42**, 641-673. doi: 10.1016/0967-0637(95)00021-W.

Oze, C., Bird, D.K., Fendorf, S. (2007). Genesis of hexavalent chromium from natural sources in soil and groundwater. *Proc. Nat. Acad. Sci. USA*. **104**(16), 6544-6549. doi: 10.1073/pnas.0701085104.

Pettine, M., D'Ottone, L., Campanella, L., Millero, F.J., Passino, R. (1998). The reduction of chromium (VI) by iron (II) in aqueous solutions. *Geochim. Cosmochim. Act*. **62**(9), 1509-1519. doi: 10.1016/S0016-7037(98)00086-6.

Quay, P., Cullen, J., Landing, W., Morton, P. (2015). Processes controlling the distributions of Cd and PO_4 in the ocean. *Glob. Biogeochem. Cy*. **29**(6), 830-841. doi: 10.1002/2014GB004998.

Rauschenberg, S. & Twining, B.S. (2015). Evaluation of approaches to estimate biogenic particulate trace metals in the ocean. *Mar. Chem*. **171**, 67-77. doi: 10.1016/j.marchem.2015.01.004.

Remmelzwaal, S.R.C., Sadekov, A.Y., Parkinson, I.J., Schmidt, D.N., Titelboim, D., Abramovich, S., Roepert, A., Kienhuis, M., Polerecky, L., Goring-HArford, H., et al. (2019). Post-depositional overprinting of chromium in foraminifera. *Earth Planet Sci Let*. **515**, 100-111. doi: 10.1016/j.epsl.2019.03.001.

Rickli, J., Janssen, D.J., Hassler, C., Ellwood, M.J., Jaccard, S.L. (2019). Chromium biogeochemistry and stable isotope distribution in the Southern Ocean. *Geochim. Cosmochim. Act*. **262**, 188-206. doi: 10.1016/j.gca.2019.07.033.

Rudnick, R.L. & Gao, S. (2003). 3.01 - Composition of the Continental Crust. Editor(s): H.D. Holland, K.K. Turekian, In Treatise on Geochemistry, Pergamon, Oxford, p. 1-64. doi: 10.1016/B0-08-043751-6/03016-4.

Rue, E.L., Smith, G.J., Cutter, G.A., Bruland, K.W. (1997). The response of trace element redox couples to suboxic conditions in the water column. *Deep Sea Res. I*. **44**(1), 113-134. doi: 10.1016/S0967-0637(96)00088-X.

684 Scheiderich, K., Amini, M., Holmden, C., Francois R. (2015) Global variability of chromium isotopes in
685 seawater demonstrated by Pacific, Atlantic, and Arctic Ocean samples. *Earth Planet. Sci. Lett*. **423**,
686 87–97. doi: 10.1016/j.epsl.2015.04.030.
687 Schlitzer, R., Anderson, R.F., Dodas, E.M., Lohan, M., Geibert, W., Tagliabue, A., Bowie, A., Jeandel, C.,
688 Maldonado, M., et al. (2018). The GEOTRACES Intermediate Data Product 2017. *Chem. Geol*. **493**,
689 210-233. doi: 10.1016/j.chemgeo.2018.05.040.
690 Schoenberg, R., Zink, S., Staubwasser, M., von Blanckenburg, F. (2008). The stable Cr isotope inventory
691 of solid Earth reservoirs determined by double spike MC-ICP-MS. *Chem Geol*. **249**, 294-306. doi:
692 10.1016/j.chemgeo.2008.01.009.
693 Semeniuk, D.M., Maldonado, M.T., Jaccard, S.L. (2016) Chromium uptake and adsorption in marine
694 phytoplankton - Implications for the marine chromium cycle. *Geochim. Cosmochim. Acta*. **184**, 41-
695 54. doi: 10.1016/j.gca.2016.04.021.
696 Shaw, T.J., Gieskes, J.M., Jahnke, R.A. (1990). Early diagenesis in differing depositional environments:
697 The response of transition metals in pore water. *Geochim. Cosmochim. Act*. **54**(5), 1233-1246. doi:
698 10.1016/0016-7037(90)90149-F.
699 Sloyan, B.M. & Rintoul, S.R. (2001). The Southern Ocean Limb of the Global Deep Overturning
700 Circulation. *J Phys. Oc*. **31**(1), 143-173. doi: 10.1175/1520-
701 0485(2001)031<0143:TSOLOT>2.0.CO;2.
702 Suga, T. & Taley, L.D. (1995). Antarctic Intermediate Water circulation in the tropical and subtropical
703 South Atlantic. *J. Geophys. Res. Oc*. **100**(C7), 13441-13453. doi: 10.1029/95JC00858.
704 Talley, L.D., Pickard, G.L., Emery, W.J., Swift, J.H. (2011). Chapter 13 - Southern Ocean. In Descriptive
705 Physical Oceanography (Sixth Edition). Editor(s): L.D. Talley, G.L. Pickard, W.J. Emery, J.H. Swift,
706 Academic Press, London, p. 437-471. doi: 10.1016/B978-0-7506-4552-2.10013-7.
707 Tréguer, P.J. & de la Rocha, C.L. (2013). The World Ocean Silica Cycle. *An. Rev. Mar. Sci*. **5**, 477-501.
708 doi: 10.1146/annurev-marine-121211-172346.
709 Twining, B.S. & Baines, S.B. (2013). The trace metal composition of marine phytoplankton. *An. Rev. Mar.*
710 *Sci*. **5**, 191-215. doi: 10.1146/annurev-marine-121211-172322.
711 van der Weijden, C.H. & Reith, M. (1982). Chromium(III) — chromium(VI) interconversions in seawater.
712 *Mar. Chem*. **11**(6), 565-572. doi: 10.1016/0304-4203(82)90003-2.
713 Vance, D., Little, S.H., de Souza, G.F., Khatiwala, S., Lohan, M.C., Middag, R. (2017). Silicon and zinc
714 biogeochemical cycles coupled through the Southern Ocean. *Nat. Geosci*. **10**, 202-206. doi:
715 10.1038/ngeo2890.

Wanner, C., & Sonnenthal, E.L. (2013). Assessing the control on the effective kinetic Cr isotope fractionation factor: A reactive transport modeling approach. *Chem. Geol*. **337-338**, 88–98. doi: 10.1016/j.chemgeo.2012.11.008.

Zink, S., Schoenberg, R., Staubwasser, M. (2010). Isotopic fractionation and reaction kinetics between Cr(III) and Cr(VI) in aqueous media. *Geochim. Cosmochim. Act*. **74**(20). doi: 10.1016/j.gca.2010.07.015.

Supplemental references not appearing in the main text

Andrews, D. & Bennett, A. (1981). Measurements of diffusivity near the sediment-water interface with a fine-scale resistivity probe. *Geochim. Cosmochim. Act*. **45**(11), 2169-2175. doi: 10.1016/0016-7037(81)90069-7

Baars, O., Abouchami, W., S. J.G. Galer, Boye, M., and Croot, P.L, 2014. Dissolved cadmium in the Southern Ocean: Distribution, speciation, and relation to phosphate. *Limnol. Oceanogr*. **59**, 385–399. doi: 10.4319/lo.2014.59.2.0385.

Conway, T.M., John, S.G., (2015). The cycling of iron, zinc and cadmium in the North East Pacific Ocean – Insights from stable isotopes. *Geochim. Cosmochim. Act*. **164**, 262-283. doi: 10.1016/j.gca.2015.05.023.

Ellwood, M.J., Bowie, A.R., Baker, A., Gault-Ringold, M., Hassler, C., Law, C.S., Maher, W.A., Marriner, A., Nodder, S., et al. (2018). Insights into the biogeochemical cycling of iron, nitrate, and phosphate across a 5300 km South Pacific Zonal Section (153°E–150°W). *Glob. Biogeochem. Cy*. **32**, 187-207. doi: 10.1002/2017GB005736.

Emerson, S., & Hedges, J. (2008). Chemical Oceanography and the Marine Carbon Cycle. Cambridge University Press, Cambridge, p. 266. doi: 10.1017/CBO9780511793202.

Henry, T., Robinson, C., Haumann, F.A., Thomas, J., Hutchings, J., Schuback, N., Tsukernik, M., Leonard, K. (2020). Physical and biogeochemical oceanography data from Conductivity, Temperature, Depth (CTD) rosette deployments during the Antarctic Circumnavigation Expedition (ACE). (Version 1.1) [Data set]. Zenodo. doi: 10.5281/zenodo.3813646.

Janssen, D.J., Abouchami, W., Galer, S.J.G., Cullen, J.T. (2017). Fine-scale spatial and interannual cadmium isotope variability in the subarctic northeast Pacific. *Earth Planet. Sci. Lett*. **472**, 241-252. doi: 10.1016/j.epsl.2017.04.048

Janssen, D.J., Sieber, M., Ellwood, M.J., Conway, T.M., Barrett, P.M., Chen, X., de Souza, G.F., Hassler, C., Jaccard, S.L. (2020b). Trace metal and nutrient dynamics across broad biogeochemical gradients in the Indian and Pacific sectors of the Southern Ocean. *Mar. Chem*. **221**, 103773. doi: 10.1016/j.marchem.2020.103773.

Kalvelage, T, Krahmann, G., Tanhua, T. (2012). Hydrochemistry during METEOR cruise M77/3. [Data set]. IFM-GEOMAR Leibniz-Institute of Marine Sciences, Kiel University, PANGAEA, doi: 10.1594/PANGAEA.793154.

Krahmann, G. (2012a). Physical oceanography during METEOR cruise M77/3. [Data set] IFM-GEOMAR Leibniz-Institute of Marine Sciences, Kiel University, PANGAEA. doi: 10.1594/PANGAEA.777255

Krahmann, G. (2012b). Physical oceanography during METEOR cruise M77/4. [Data set]. IFM-GEOMAR Leibniz-Institute of Marine Sciences, Kiel University, PANGAEA. doi: 10.1594/PANGAEA.777907.

Li, Y.H. & Gregory, S. (1974). Diffusion of ions in sea water and in deep-sea sediments. *Geochim. Cosmochim. Act*. **38**(5), 703-714. doi: 10.1016/0016-7037(74)90145-8.

Tanhua, T., Karstensen, J., Malien, F., Ryabenko, E., Kock, A. (2012). Hydrochemistry during METEOR cruise M77/4. [Data set]. IFM-GEOMAR Leibniz-Institute of Marine Sciences, Kiel University, PANGAEA. doi: 10.1594/PANGAEA.793153.

Ullman, W.J., & Aller, R.C. (1982). Diffusion coefficients in nearshore marine sediments. *Lmnol. Oceanogr*. **27**(3), 552-556. doi: 10.4319/lo.1982.27.3.0552.

Potential sources	Sediment phase	Cr per phase	Cr contributed to bulk sediment	Cr needed
	% of bulk	ppm	ppm	ppm
Organic matter/ Surface phytoplankton	1	11.7	0.1	49
$CaCO_3$	76	0.1	0.08	
Lithogenic material/ Upper continental crust	20	90	18	

766 **Table 1: Mass balance for sedimentary Cr**.

767 Potential sources of Cr in marine sediments are compared to evaluate the origin of the benthic Cr flux.
768 Sediment phase percentages (organic matter, $CaCO_3$, lithogenic material) are averages from the upper 4 cm
769 (Table S6). Cr per phase is the concentration expected in each individual phase (surface phytoplankton:
770 Martin & Knauer, 1973; $CaCO_3$: Remmelzwaal et al., 2019; upper continental crust: Rudnick & Gao, 2003).
771 Cr contributed to bulk sediment is the Cr that each phase would contribute to the bulk sediment
772 concentration, based on sediment phases and Cr per phase. Cr needed is the required [Cr] in the sediments
773 (i.e. the [Cr] of particles that must be delivered to sediments) to explain the calculated diffusive Cr flux
774 from sediments (3.2 nmol cm^{-2} yr^{-1}, Table S6), assuming a sedimentation rate in the region of 2 cm ka^{-1}
775 (e.g. Cochran & Osmond, 1976). A sedimentation rate on the higher side of regional observations was
776 chosen to give a minimum estimate of the Cr needed. The assumed sediment density is 1.7 g cm^{-3}.

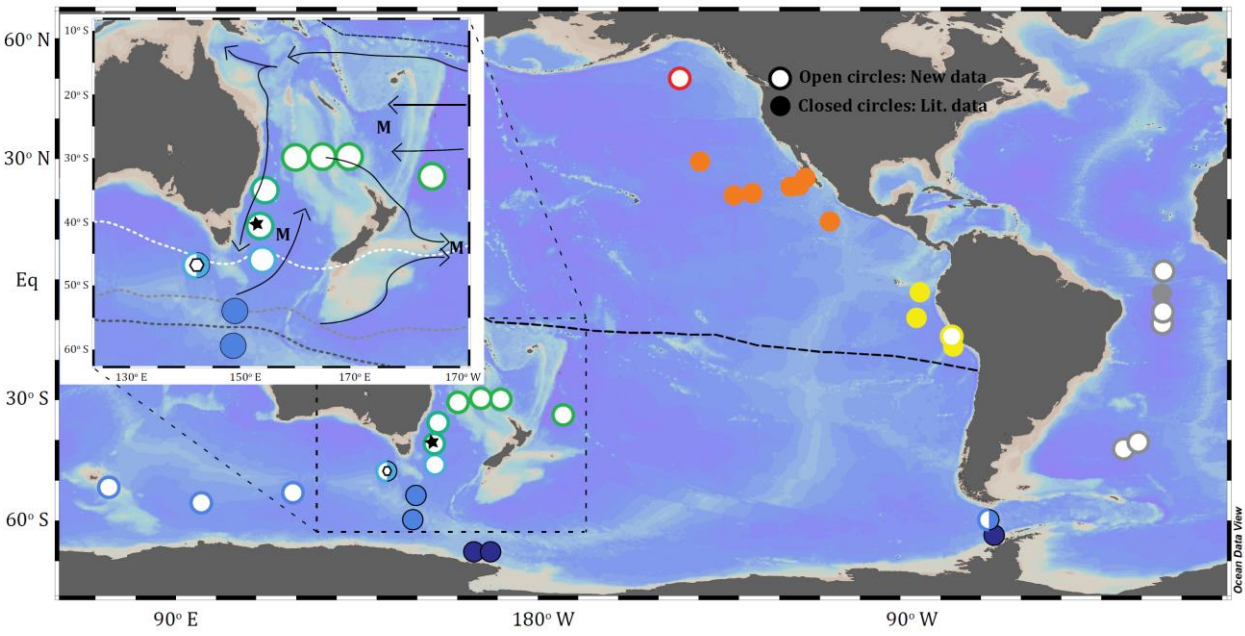

Figure 1: Map of sampling locations.

Station locations are shown for new data (open circles) and literature data (filled circles). Split circles indicate locations with both new and literature data. Full data tables can be found in the supplemental material. The black star denotes the location of the multicore site, where bottom and pore waters were collected. The northernmost extent of AAIW as a primary water mass component in the Pacific Ocean (Bostock et al., 2013), is shown as a dashed black line. The inset shows the subantarctic Southern Ocean, the Tasman Sea (located between Australia and New Zealand) and the subtropical southwestern Pacific, the sites for most of the new data. The flow paths of AAIW are shown in the inset as black arrows, and M denotes regions of enhanced AAIW mixing (Bostock et al., 2013). Dashed white and grey lines indicate representative fronts of the Southern Ocean (white – the Subtropical Front, light grey – the Subantarctic Front, dark grey – the Polar Front; Orsi et al., 1995).

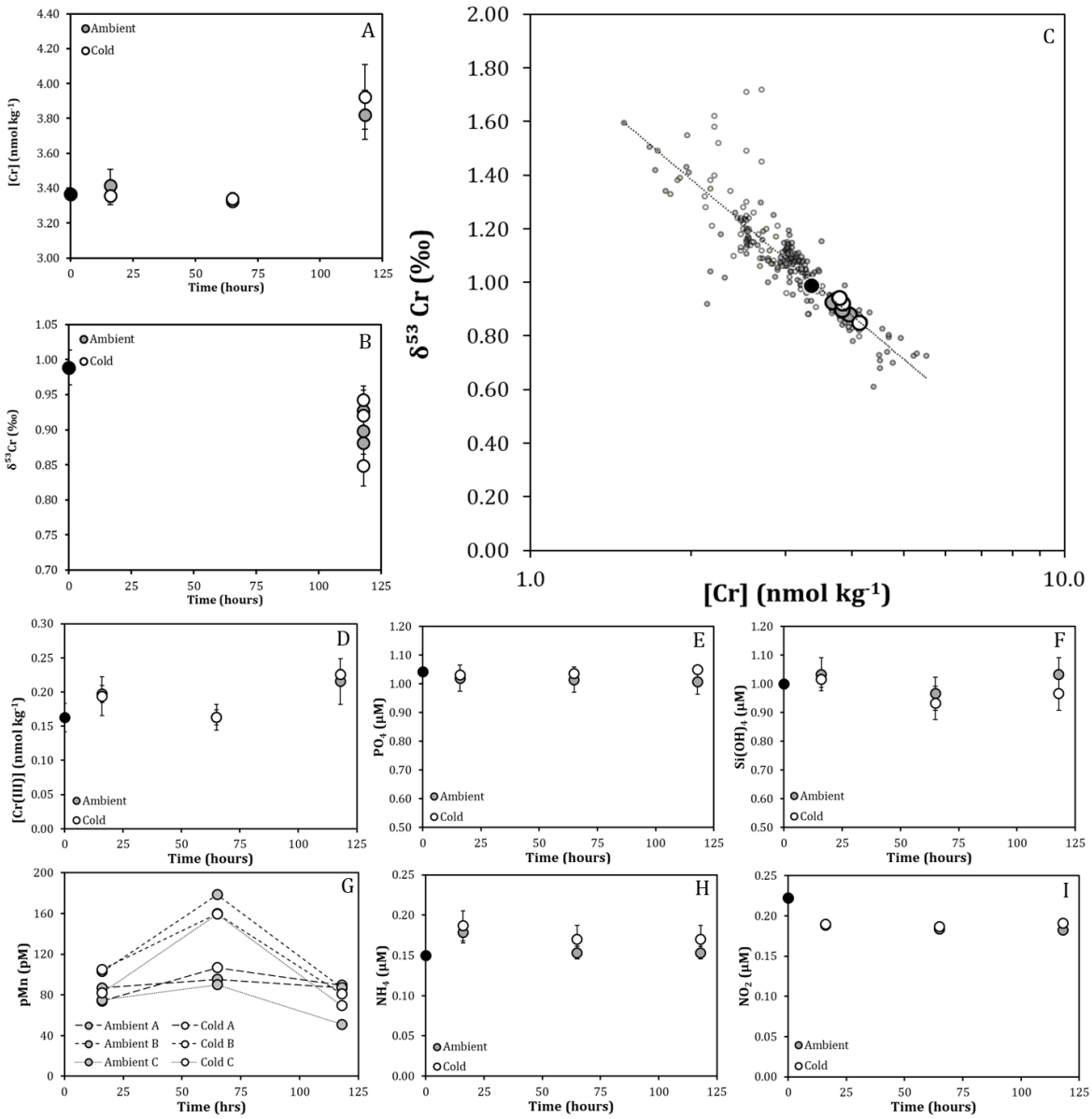

Figure 2: Regeneration incubation data.

Data for dissolved Cr concentrations (panel A), stable isotope composition (panel B) and redox speciation (panel D) are presented for regeneration incubation 3, along with macronutrients (PO_4: panel E; $Si(OH)_4$: panel F; NH_4: panel H; NO_2: panel I) and pMn (panel G). Incubation sample $\delta^{53}Cr$ and [Cr] are shown over the global array of oceanic data with a trendline fit to all the data (Panel C), demonstrating the alignment of released Cr along the global distribution. The ambient temperature (4° C) treatment is shown as grey circles and the 1° C treatment as white circles, with the initial dissolved water shown as a black circle.

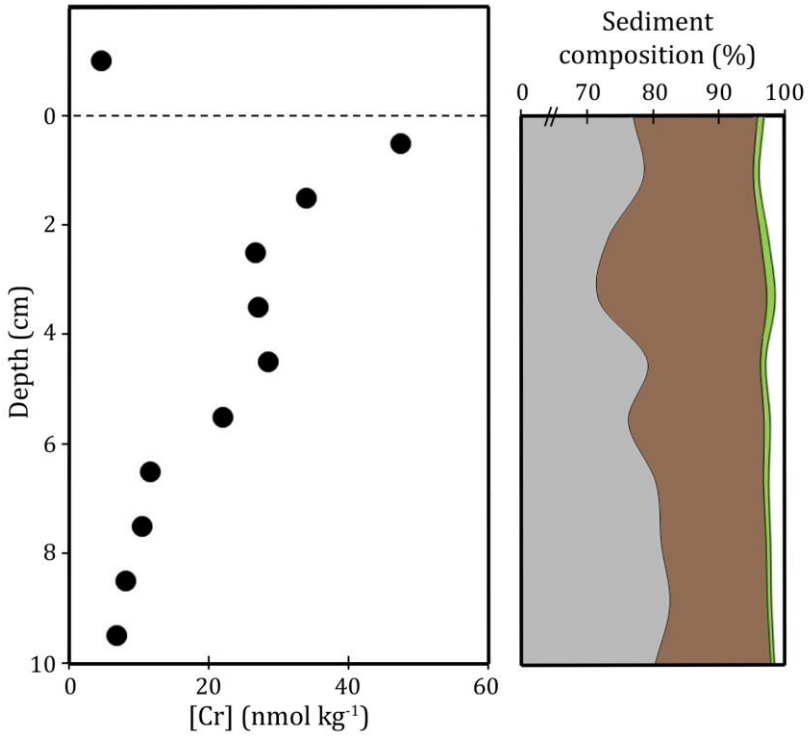

Figure 3: Pore water [Cr] profile.

The left panel shows pore water dissolved [Cr] with depth in the sediment. Concentrations represent pore water concentrations in sample intervals of 1 cm. Dissolved bottom water [Cr] is shown from a sample collected approximately 10 cm above the sediment-water interface (shown as a dashed line). Uncertainty is smaller than the symbol size. Note that the y axis scale above the sediment-water interface is different from the scale below the interface. The right panel shows bulk sediment composition for the same core and sediment intervals as pore water data ($CaCO_3$ – grey, lithogenic material – brown, organic matter – green; see supplemental section 3.3 and Table S7). The x axis scale has a break between 0% and 70%.

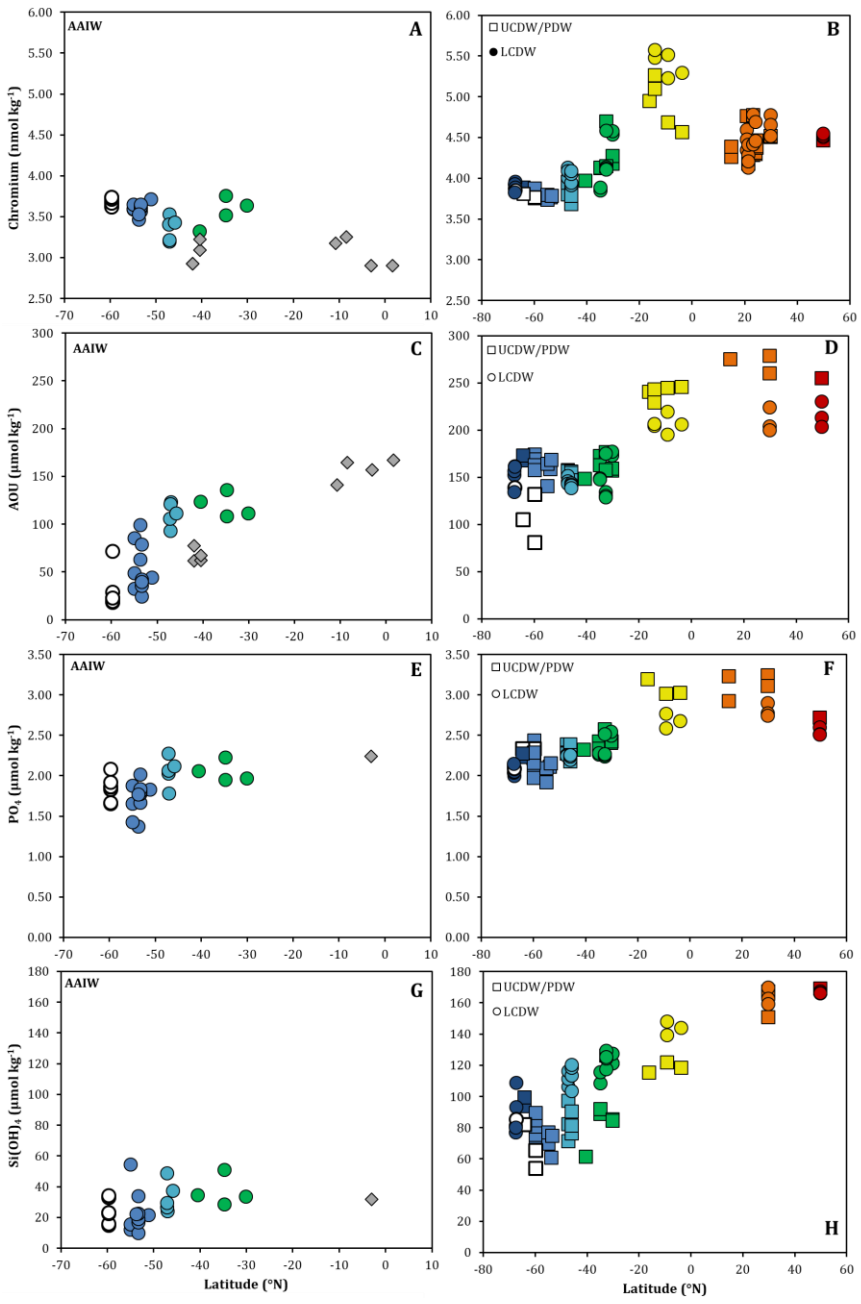

808

809 **Figure 4: Chromium and macronutrient concentrations and AOU along intermediate and deep water**

810 **circulation.**

811 Modification of deep water [Cr] is shown, along with parameters associated with the regeneration of organic

812 material ([PO_4], AOU) and dissolution of plankton skeletal/frustule phases ([$Si(OH)_4$]). Panels on the left

813 show AAIW (circles – Southern and Pacific Ocean data, diamonds – Atlantic Ocean data) while panels on

814 the right show Southern and Pacific Ocean UCDW, PDW and LCDW, with UCDW and PDW in circles

and LCDW in squares. Open circles denote samples with Antarctic Surface Water or Winter Water contributions. Colors match sampling locations shown in Figures 1 and S2, and full data and sources are shown in Tables S8-S10. Direct comparisons between [Cr] and AOU, PO_4 and $Si(OH)_4$ are shown in Figure 5. Note the different x axis ranges for left and right panels.

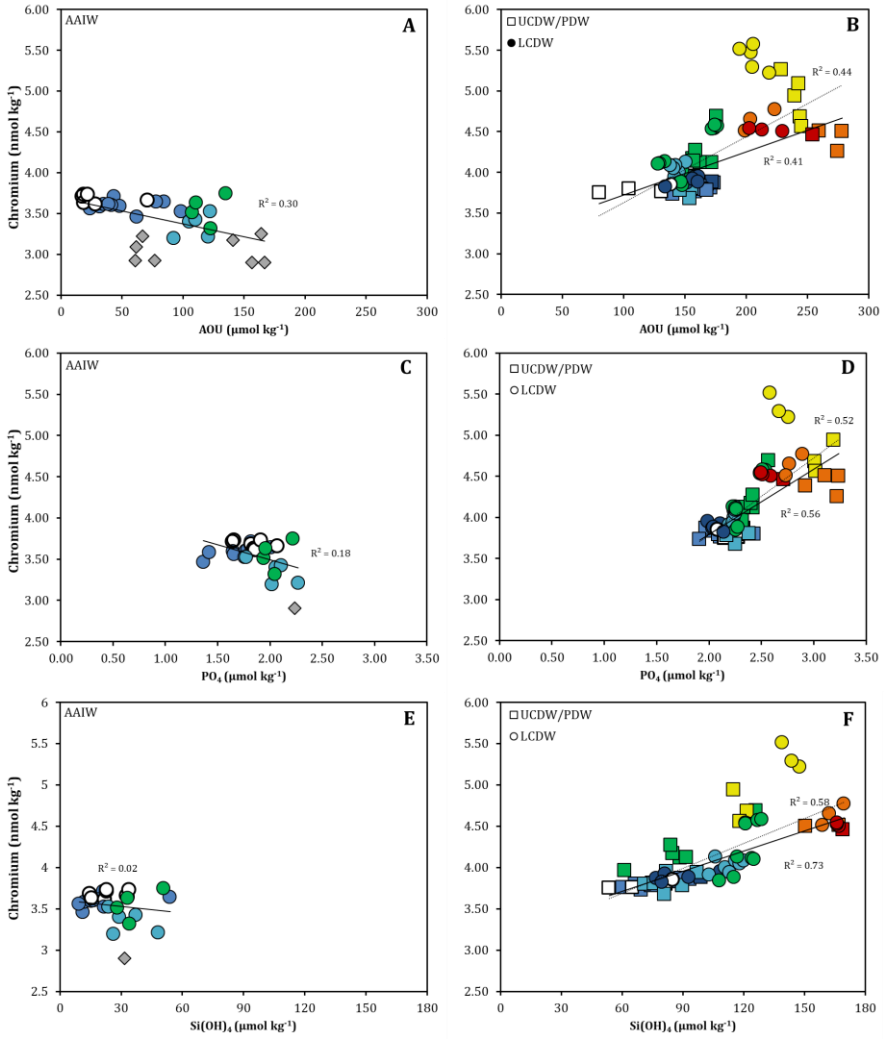

Figure 5: Chromium–nutrient and Cr–AOU cross plots.

Dissolved Cr is shown compared to AOU (A, B), PO_4 (C, D) and $Si(OH)_4$ (E, F) for the intermediate (A, C, E) and deepwater (B, D, F) dataset to highlight decoupling of Cr from tracers of organic matter respiration and regeneration of organic-associated macronutrients (AOU, PO_4). Symbols follow those used in Figure 4.

826

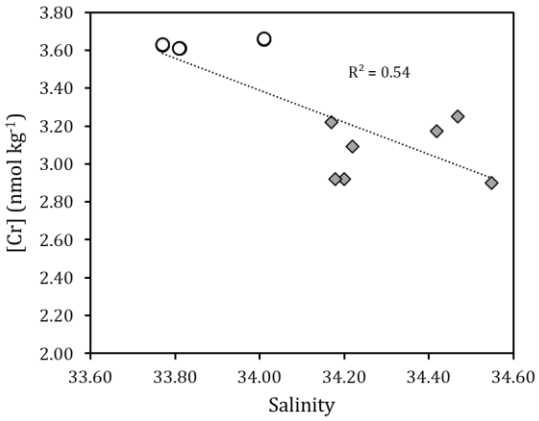

827

828 **Figure 6: The impact of mixing on [Cr] in AAIW.**

829 Chromium concentrations are shown with salinity for AAIW samples in the Drake Passage (open circles)

830 and the Atlantic Ocean (grey diamonds).

831

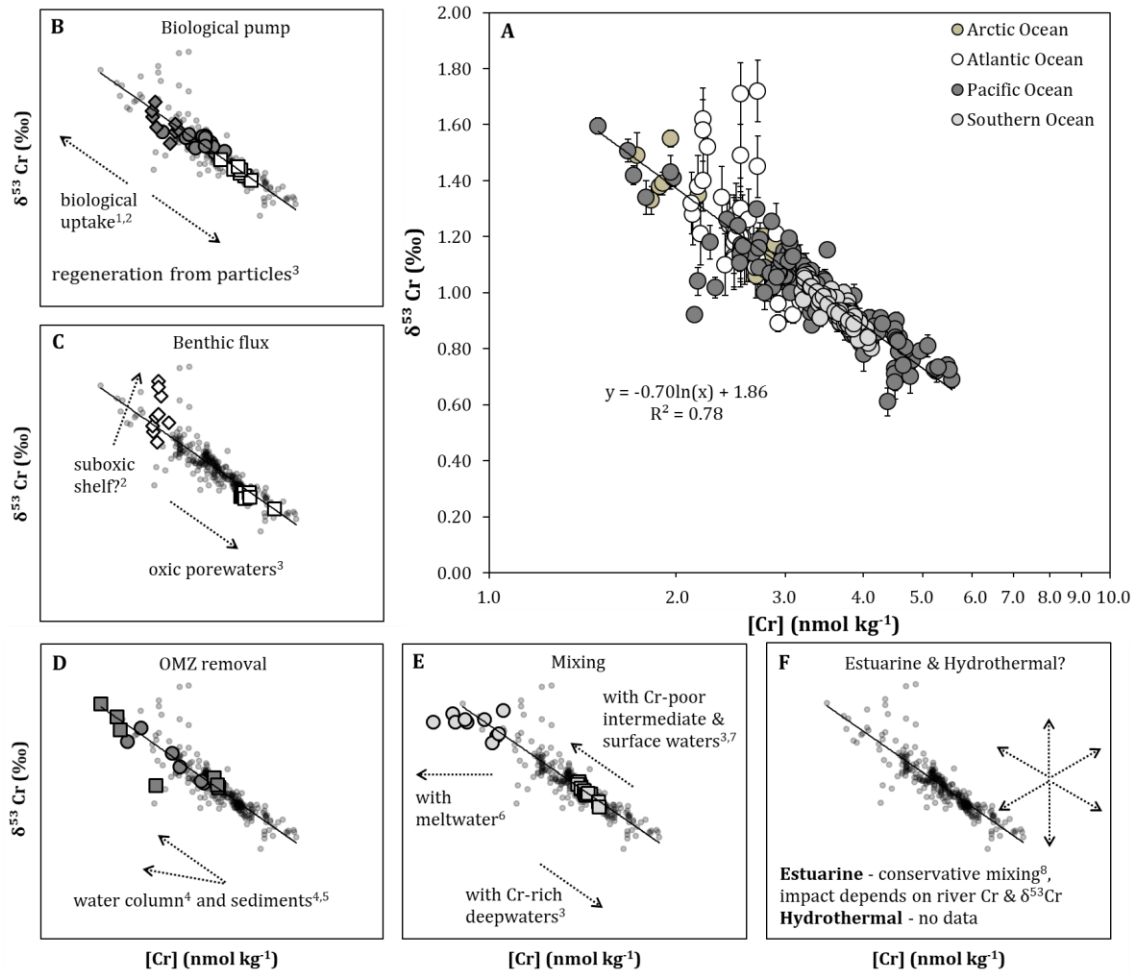

Figure 7: Toward a mechanistic understanding of the global ocean Cr cycle.

The global array of open ocean [Cr] and δ^{53}Cr data is shown (panel A) along with specific subsets of data highlighted to demonstrate how different processes drive the global distribution. References for these subsets are shown by superscripts. Processes which act to increase [Cr] are shown in white and processes which act to decrease [Cr] are shown in dark grey. Mixing, which may increase or decrease [Cr] depending on the point of reference, is shown in light grey. Panel B shows processes within the biological pump (surface uptake, export of biogenic particles, and regeneration at depth). Panel C shows benthic Cr fluxes. Panel D shows Cr removal in OMZs, which may follow the global trend or deviate slightly. Panel E shows mixing processes. Panel F shows processes which are unconstrained at present (hydrothermal fluxes) or which may have variable impact depending on local characteristics (riverine [Cr] and δ^{53}Cr, estuarine mixing). The axes and ranges of all panels are identical. Data from Moos & Boyle (2019) as well as the

following studies were used: [1]Janssen et al., 2020 (dark grey circles, panel B); [2]Goring-Harford et al., 2018 (dark grey diamonds, panel B; white diamonds, panel C); [3]This study (white squares, panels B & C), [4]Moos et al., 2020 (dark grey circles, panel D); [5]Nasemann et al., 2020 (dark grey squares, panel D); [6]Scheiderich et al., 2015 (light grey circles, panel E), [7]Rickli et al., 2019 (light grey squares, panel E), [8]Goring-Harford et al., 2020.